



## The onboard imagers for the Canadian ACE SCISAT-1 mission

K. L. Gilbert,<sup>1</sup> D. N. Turnbull,<sup>2</sup> K. A. Walker,<sup>3</sup> C. D. Boone,<sup>1</sup> S. D. McLeod,<sup>1</sup> M. Butler,<sup>1</sup> R. Skelton,<sup>1</sup> P. F. Bernath,<sup>4</sup> F. Chateaufneuf,<sup>5</sup> and M.-A. Soucy<sup>5</sup>

Received 29 June 2006; revised 7 February 2007; accepted 5 March 2007; published 21 June 2007.

[1] The Atmospheric Chemistry Experiment (ACE) onboard the Canadian Space Agency's SCISAT-1 satellite has been in orbit since August of 2003. Its broad objective is to study the problem of stratospheric ozone depletion, particularly in the Arctic. The main instruments are two spectrometers, one an infrared Fourier Transform Spectrometer and the other a dual optical spectrophotometer sensitive in the UV and visible. Also included are two filtered imagers used to measure altitude profiles of atmospheric extinction and detect thin clouds. The nominal center wavelengths of the filters are 525 nm for the visible (VIS) imager and 1020 nm for the near-infrared (NIR) imager. With the decommissioning of other satellite instruments used to monitor global aerosols [i.e., Stratospheric Aerosol and Gas Experiment II (SAGE II), SAGE III, Polar Ozone and Aerosol Measurement (POAM) III, Halogen Occultation Experiment (HALOE)], the imagers provide much needed continuity in this data record. The data product from the imagers is still, however, in a preliminary state. Funding restrictions in the prelaunch period were responsible for an incomplete characterization of the imagers' optics and electronics and prevented corrections being made for the problems found during testing. Postlaunch data analysis to correct for image artifacts is ongoing. A comparison with coincidental measurements from SAGE II shows that systematic errors from the preliminary analysis are within 5 and 20% for the VIS and NIR imagers, respectively, for uninverted profiles of optical depth. Despite the preliminary nature of the imager results, a paper describing the imagers and the initial operational data processing code is timely because the data are already being used.

**Citation:** Gilbert, K. L., D. N. Turnbull, K. A. Walker, C. D. Boone, S. D. McLeod, M. Butler, R. Skelton, P. F. Bernath, F. Chateaufneuf, and M.-A. Soucy (2007), The onboard imagers for the Canadian ACE SCISAT-1 mission, *J. Geophys. Res.*, 112, D12207, doi:10.1029/2006JD007714.

### 1. Introduction

[2] The Atmospheric Chemistry Experiment (ACE) was launched on 12 August 2003, the first of the Canadian Space Agency's small scientific satellite missions (SCISAT-1). ACE circles the Earth at an altitude of 650 km with an orbital inclination of 74°. It has a number of purposes [see Bernath *et al.*, 2005], chief among them being to illuminate the chemical and physical processes controlling ozone in the upper troposphere and stratosphere at high latitudes. It does this by measuring altitude profiles of a number of atmospheric species involved in ozone chemistry, as well as tempe-

perature, pressure, and ambient density profiles from ~5–150 km. One of the other goals of the mission is to measure aerosols and clouds in order to reduce the uncertainties in their effects on the global energy balance. Solar occultation is the primary observation technique used by the onboard instruments, which consist of a high-resolution infrared Fourier Transform spectrometer (ACE-FTS), a dual optical spectrophotometer (MAESTRO), and the two filtered imagers that are the subject of this paper.

[3] ACE-FTS covers the spectral range of 750–4400 cm<sup>-1</sup> with a resolution of 0.02 cm<sup>-1</sup> and provides profiles of atmospheric constituents with an altitude resolution of ~4 km. MAESTRO stands for Measurement of Aerosol Extinction in the Stratosphere and Troposphere by Occultation [McElroy *et al.*, 2007] although it also measures ozone, nitrogen dioxide, and some other trace compounds. Its spectral range is between 285–1030 nm with a resolution of 1–2 nm, depending on wavelength, and it has an altitude resolution of 1–2 km.

[4] The imagers play both a scientific and a support role in the mission. They support the mission by providing pointing information, inasmuch as the fields of view of the onboard spectrometers have been coregistered with

<sup>1</sup>Department of Chemistry, University of Waterloo, Waterloo, Ontario, Canada.

<sup>2</sup>Department of Physics and Astronomy, The University of Western Ontario, London, Ontario, Canada.

<sup>3</sup>Department of Physics, University of Toronto, Toronto, Ontario, Canada.

<sup>4</sup>Department of Chemistry, University of York, York, United Kingdom.

<sup>5</sup>ABB, Remote Sensing Industry, Québec City, Québec, Canada.

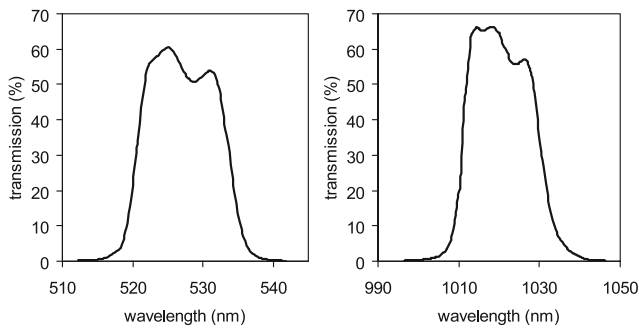


**Figure 1.** The transmission of the imager filters as a function of wavelength is shown for the VIS imager on the left and for the NIR imager on the right.

specific imager pixels. The imagers view the entire sun, and therefore the portion of the sun viewed by each spectrometer is accurately known. They were also key to the characterization of the onboard suntracker, which directs sunlight to all the instruments.

[5] The scientific role of the imagers is to provide atmospheric extinction profiles at the nominal wavelengths of the two filters: 525 nm for the visible (VIS) imager and 1020 nm for the near-infrared (NIR) imager. Extinction at these wavelengths is caused mainly by Rayleigh scattering, aerosols and clouds, and in the case of the 525-nm channel, by ozone as well. The wavelengths were selected to match two of the seven channels of NASA's Stratospheric Aerosol and Gas Experiment (SAGE) II instrument [Russell and McCormick, 1989]. SAGE II had been providing atmospheric aerosol extinction profiles, among other things, since the mid-1980s but was turned off in September 2005 because of old age. Until recently, some other non-imaging satellite instruments were monitoring aerosols and clouds at the same wavelengths using the solar occultation technique, namely the Polar Ozone and Aerosol Measurement (POAM) III instrument [Lucke et al., 1999] and SAGE III [Thomason and Taha, 2003]. The Halogen Occultation Experiment (HALOE) [Russell et al., 1993] also provided aerosol extinction profiles using solar occultation measurements but observed at longer wavelengths than the others. These instruments are no longer in operation. Thus both the imagers and MAESTRO on ACE will help provide continuity in the long-term data record of global aerosol abundances [see, e.g., Fromm et al., 2003].

[6] Imagers have a couple of advantages over non-imaging instruments for this application. They offer flexibility in the spatial resolution of their profiles depending on the number of pixels binned for analysis. Thus trade-offs can be made between higher spatial resolution and a higher signal-to-noise ratio obtained from binning pixels. Another advantage of using image data is that the transmission values are more reliable because it is known where on the sun an intensity is being measured; that is, inaccuracies introduced by viewing different parts of the solar disk, which may be differentially limb-darkened, are avoided.

[7] The images are already being put to use in the detection and identification of cirrus and polar stratospheric

clouds [Dodion et al., 2007], and their atmospheric extinction profiles are supporting the remote sensing of biomass burning [Rinsland et al., 2006]. Because ACE imager data are now in demand and still in a preliminary processing state, it seems necessary to provide a description of the imagers so that the data may be better understood. This is particularly important because the imagers suffered the brunt of program budget restrictions during and after the build period, as they are lower priority instruments compared to ACE-FTS and MAESTRO. They were left with some handicaps that must be appreciated before their data can be properly interpreted.

[8] A brief description of the imagers is given in the next section followed by the results of their characterization both pre- and postlaunch. The preliminary data processing procedure to produce atmospheric extinction profiles is then outlined, and a comparison is made with coincident SAGE II measurements in order to evaluate their performance.

## 2. Instrument Description

[9] The two ACE imagers are supposed to be identical except for their respective filters (Figure 1), which were made by Andover Corporation. The VIS filter is centered at 527.11 nm and has a full width at half maximum (FWHM) bandwidth of 13.28 nm. The NIR filter is centered at 1020.55 nm with a FWHM bandwidth of 19.44 nm.

[10] The imagers are integrated into a unit also containing the FTS, suntracker, and input optics, all built or supplied by ABB-Bomem in Québec City. Incoming sunlight reaching the imager assembly first encounters a neutral density filter which prevents saturation of the detectors facing the unattenuated high sun (Figure 2). After passing through some lenses, the light is split by a dichroic element and directed to each imager. The NIR imager receives the transmitted light, and the VIS receives the reflected light. The NIR and VIS images are therefore mirror reflections of each other. The nominal field of view is 30 mrad, which is roughly three times wider than the sun's apparent diameter of about 9 mrad.

[11] Each imager consists of a complementary metal oxide semiconductor (CMOS) active pixel detector array made by Fill Factory of Mechelen, Belgium, with a protective window and associated electronics, and fronted by its filter. The imaging area on the detector comprises 256 ×

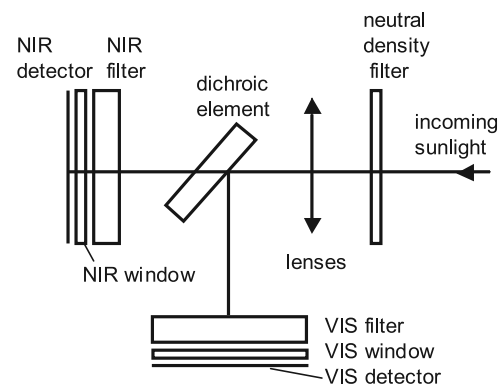


**Figure 2.** Schematic of the optics layout for the two imagers.

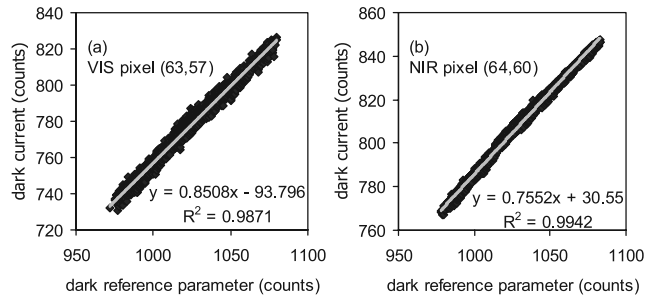


**Figure 3.** Scatterplot of the dark reference parameter versus the dark current for the pixel coregistered with the center of the FTS field of view for (a) the VIS imager and (b) the NIR imager. The dark reference parameter values cover the range measured on orbit. The straight lines are the best fits to the data.

256 square pixels on a 25-micron pitch. Each pixel contains four photodiodes to enhance the modulation transfer function and reduce photo-response nonuniformity. To the left and right of the imaging area are columns of pixels covered with a metallized layer to prevent light penetration. The signal from these pixels is averaged to provide a parameter for each image for the purpose of dark current correction, which will be described below. This parameter is called the dark reference parameter and is stored in the header of each image file. The pixels in the imaging area are binned after readout to produce an effective  $128 \times 128$  pixel array, but in practice, only  $64 \times 64$  pixels containing the sun's image are retained in order to reduce the volume of telemetry data.

[12] A  $64 \times 64$  pixel image along with a header containing imager parameters is stored in a file every 0.25 s. This image is the sum of nine faster images or frames. Each frame is taken at the longest exposure time that still gives a linear response from the detector:  $\sim 10$  ms for the VIS imager and  $\sim 11$  ms for the NIR imager. The readout time for a frame is roughly 2.5 times as long as the exposure time. The pixels are read out by rows using a double sampling technique [Razavi, 2001] to reduce the fixed pattern noise inherent in CMOS devices. A gain of 2 is applied to the voltage produced by each pixel to better fill the 10 bits of the analogue-to-digital converter and thus reduce the quantization noise [Kester, 2005].

### 3. Characterization and Performance

[13] Budget constraints at the time of the instrument build period focused effort on the two flight spectrometers. While the imagers were built according to their approved space-qualified design, no allowance was made in budget or schedule for possible modifications based on later testing. The test periods which followed were therefore more like characterization periods for the imagers, and the test equipment was optimized for the spectrometers. The instruments underwent verification testing by their builders and then science-evaluation testing by the science team.

[14] It was not possible to completely simulate flight conditions for the tests because the light sources used to simulate the sun were, of course, not as bright as the sun,

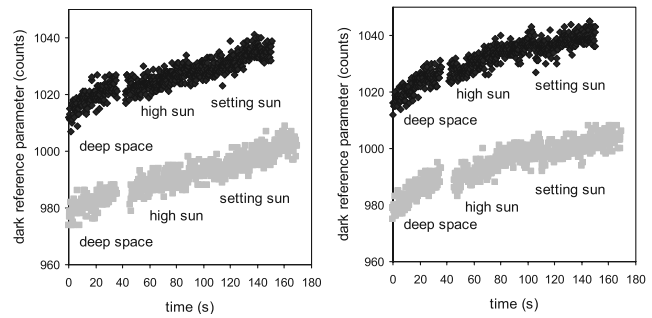


**Figure 4.** Examples of the dark reference parameter from the VIS imager (left) and the NIR imager (right) as it changes over the course of observing a sunset. The top points are from ss3006 and the bottom points from ss4822.

and produced somewhat different intensity distributions with wavelength. For the imagers, this meant that the flight settings for gain, exposure time, and the number of coadded frames per image noted in the previous section had to be determined in orbit; the combination of these settings is different from those tested on the ground. It was not possible to arrange on the ground for a spatially uniform light source that was bright enough to measure the relative response of the detector pixels to light (i.e., flat-fielding). Similarly, it was not possible to measure cross-talk between pixels, or verify the nominal field of view to subpixel precision.

[15] On the other hand, a thorough characterization on the ground of the dark current as a function of temperature, gain, and exposure times showed that the detectors function as expected in these respects. The flight characterization of dark current took place early in the mission during the science commissioning phase. The instruments have three distinct observation segments. They look at deep space, the high sun, and then the occulted or low sun during a sunset, and the same in reverse order for a sunrise. For the high and

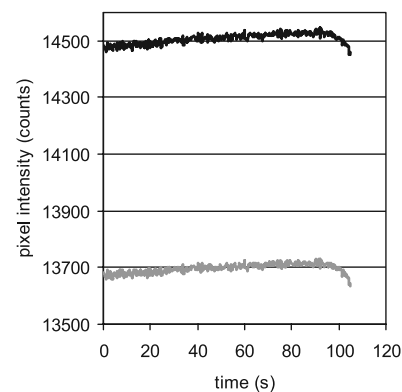


**Figure 5.** Counts from the pixel coregistered with the center of the FTS field of view during the NIR high sun image stream showing the anomalous intensity increase. The bottom trace is corrected for dark current, and the top trace is uncorrected. The drop in intensity on the right hand side marks the beginning of sunset (ss3448). A straight line provides the best fit to the upward trend.

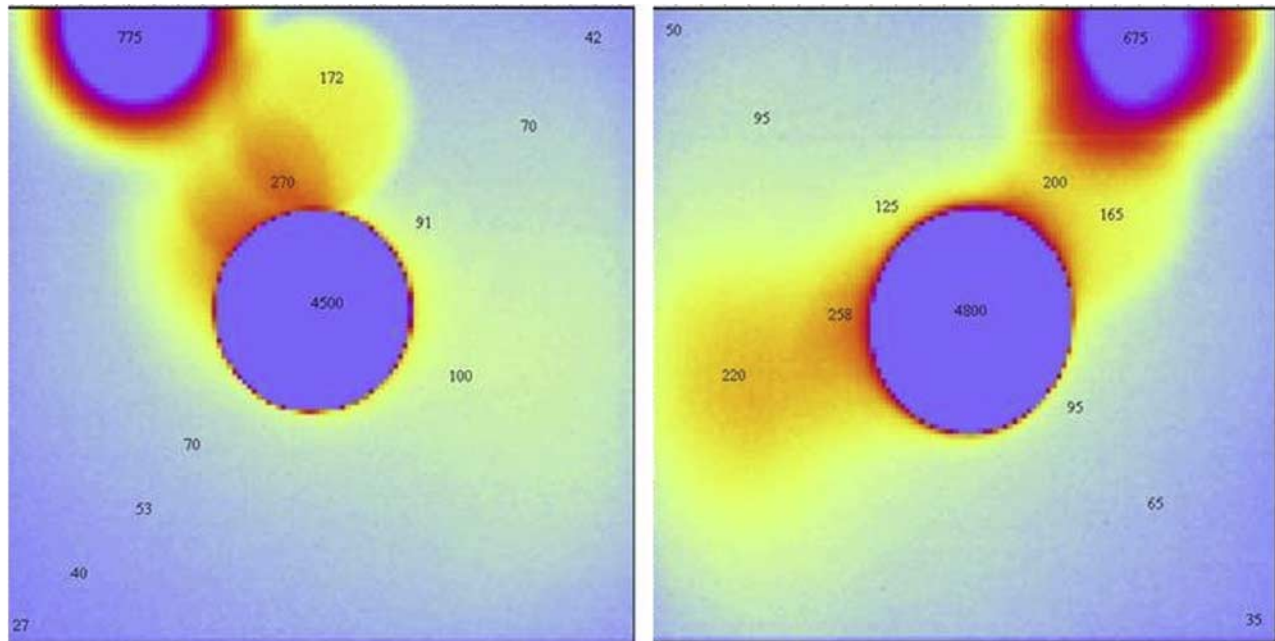


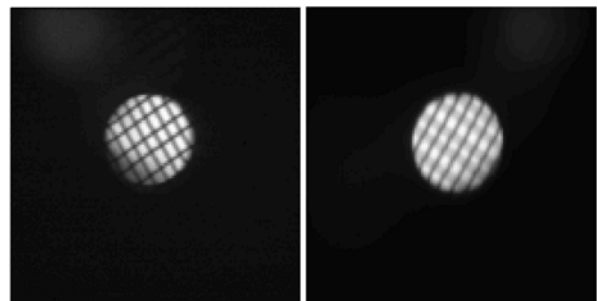
**Figure 6.** False color images of the high sun taken with the VIS imager (left) and the NIR imager (right), after correction for dark current. The annotated numbers indicate the analogue-to-digital converter (ADC) counts from various pixels. The color scheme is contrived to saturate at a medium count level in order to highlight the weaker multiple images. The strongest secondary image in the top left corner for the VIS and top right corner for the NIR is  $\sim 15\%$  of the main image intensity.

low sun images, the dark reference parameter that is stored in every image file header is an indicator of the amount of dark current present in a measurement from an image pixel. The on-orbit dark images from 30 occultations, which amount to 4260 images, were used to calibrate each pixel's dark current against the dark reference parameter (Figure 3). This turns out to be a linear relationship, although variations among detector pixels cause small variations in the slope and intercept for each pixel. This relationship is used to correct for dark current during data processing. In Figure 3, it can be seen that the dark current observed in orbit for a given pixel can vary by  $\sim \pm 7\%$  from the mean for the VIS imager and  $\sim \pm 10\%$  for the NIR imager. As the exposure time and gain setting are constant, this variation is likely due to small temperature variations. While there are no temperature sensors on the imagers, the sensor at the nearby ACE-FTS beamsplitter shows that its temperature can vary by several Kelvin for different occultations, although for any given occultation its temperature is maintained at a constant value to within several hundredths of a Kelvin.

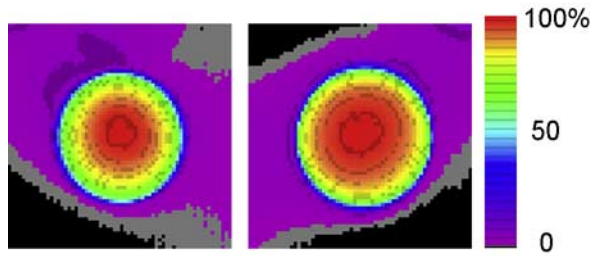
[16] An unexpected behavior of the detectors that was discovered in flight is an anomalous linear increase in detector response during an occultation (Figure 4). While the cause of this effect is not known, it apparently involves the operation of the detector itself rather than heating from the sun because it appears in the dark image stream as well as the high sun image stream. Figure 5 illustrates that the linear increase in pixel intensity persists even after dark current subtraction. The high sun image stream for each occultation is used to correct for this anomaly during data processing. The trend is deduced from the unrealistic increase in the high sun's maximum intensity, after dark current subtraction, and then extended into the low sun

image stream. In the preliminary processing code, the correction takes the form of subtracting a constant number of surplus counts from every pixel in any one image, with the number of subtracted surplus counts increasing for successive images in time according to the deduced trend.

[17] The most serious imager problems are with the optics rather than the detectors. It became apparent during testing that both imagers suffer from overlapping multiple images (Figure 6). The multiple images have been traced to reflections from the neutral density filter, which is not tilted enough with respect to the optic axis and has a nominal reflectance of 54%. There are one or two distinct, strong



**Figure 7.** Images of a mesh attenuator screen in front of a target light source taken during the test period. The VIS image is on the left, and the out-of-focus NIR image is on the right. The only difference here between the imager settings is a higher gain for the VIS imager due to the intensity distribution of the 2400°C hot blackbody light source. Note that the NIR image also appears larger and elliptical compared to the VIS.



**Figure 8.** False color reference images of the high sun for occultation ss8651. The VIS image is on the left, and the NIR is on the right.

secondary images but many more weaker reflections creating diffuse swaths of energy in the image. It is the reflected images underlying the main sun image that are most problematic because the pixels in the main sun image provide the data on atmospheric transmission. The positions of the multiple images shift when the main image appears in different parts of the imagers' field of view. Fortunately, the main image is positioned for routine operation so that the strong secondary images do not overlap it. Nevertheless, it is as yet undetermined how much signal the sum of weaker images contributes to the pixels in the main image; around the edge of the main image, the contribution is  $\sim 5\text{--}8\%$ . The problem is exacerbated as the sun image becomes deformed during an occultation; the multiple images also deform and move so that they continually overlap differently. It is difficult to construct a model that accurately describes the multiple images in order to correct for them analytically. The necessary measurements that would have furnished information on the intensities, orientations, and positions of the unwanted images were not performed on the ground because of budget restrictions; the reflectances and transmittances of the optical elements are either unknown or known only as manufacturers' specifications, and the focal length is known only imprecisely.

[18] In addition to this, the NIR imager is out of focus and produces a distorted image, for reasons that are not clear (Figure 7). Coregistration of the two imagers during the test period revealed the field of view of the NIR imager to be

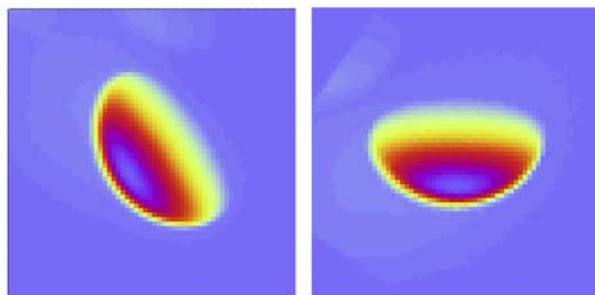


**Figure 9.** A VIS low sun image before (left) and after (right) rotation. The smallest angle that will orient the horizon parallel to the imager horizontal axis is chosen, which puts the horizon at the top of the image. The image has been corrected for dark current.

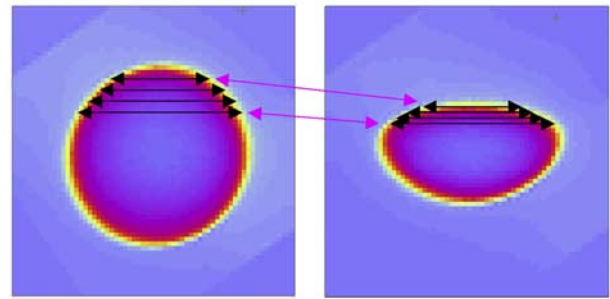


**Figure 10.** Mapping of pixels between the deformed low sun and the high sun. It is assumed that the width of the sun remains unaffected by refraction, and that the apparent deformation is strictly along the local vertical to the Earth's surface. The two images have already been rotated as part of data processing, so that all pixels in a given row have the same tangent height.

$\sim 6\%$  larger than for the VIS, but the overall image is  $\sim 10\%$  larger, not to mention elliptical.

[19] Despite these problems, the signal-to-noise ratio for the imagers is very good:  $\sim 1500$  for an image pixel at the center of the high sun after correction for dark current, compared to the design specification of 1000 for a raw image.

#### 4. Data Analysis

[20] The data-analysis procedure is still in a preliminary state, but the main steps involved follow a standard format for solar occultation measurements [see e.g., *Aikin et al.*, 1982; *Houghton et al.*, 1984]. The sequence of images taken over an occultation is analyzed to produce a profile of atmospheric transmission along the line of sight to the sun, which is then inverted to produce an altitude profile of total atmospheric extinction. Atmospheric transmission values are obtained from the ratio of the intensity of sunlight as obscured by the Earth's atmosphere to the intensity of the high sun, measured from image pixels. Each image pixel is associated with a tangent height. This is defined as the point of closest approach of a pixel's line of sight with respect to the center of the Earth. In successive images, the tangent

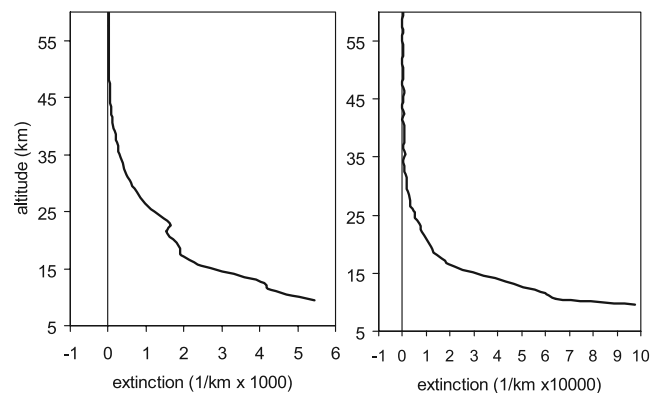


**Figure 11.** Examples of retrieved altitude profiles of atmospheric extinction for occultation ss6910, for the VIS imager on the left and the NIR imager on the right.

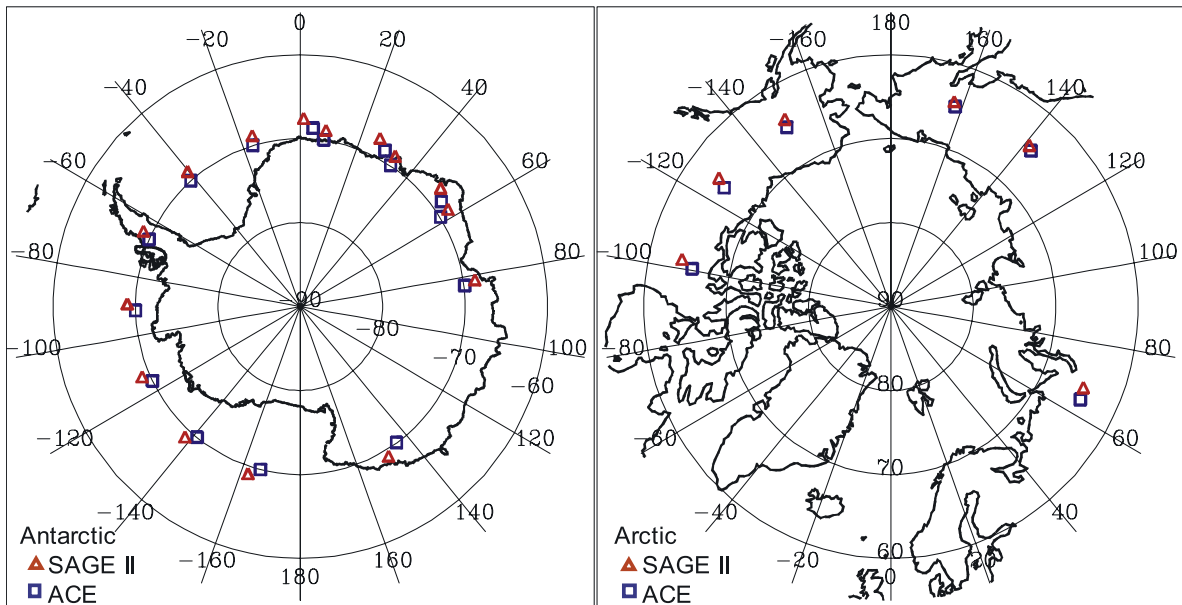


**Figure 12.** Locations of coincident SAGE II (triangles) and ACE (squares) observations made at 20 km tangent altitude in the Antarctic (left) and the Arctic (right).

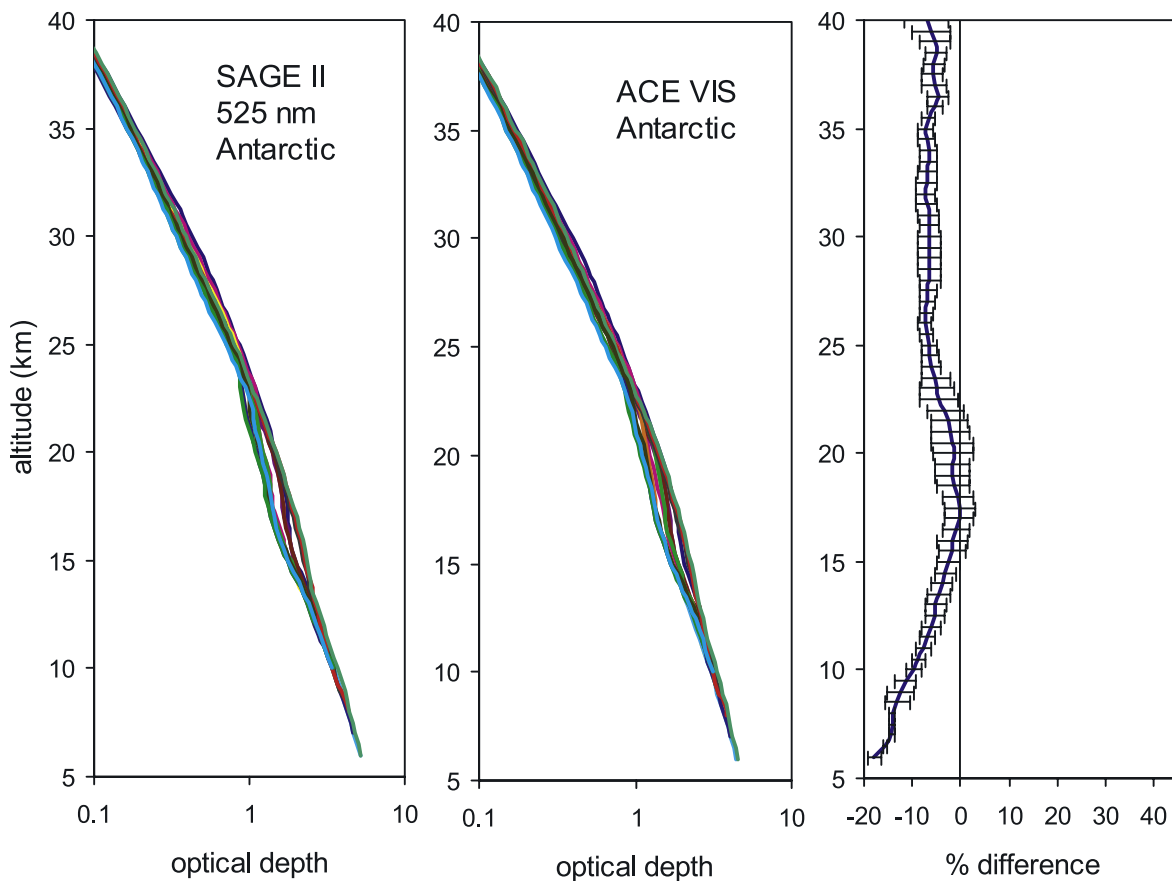


**Figure 13.** Coincident optical depth slant path profiles from the 525-nm channel of SAGE II (left) and the ACE VIS imager (middle) during November 2004 from the Antarctic. Fifteen profiles are plotted in each case. The plot on the right hand side shows the average difference between the SAGE II and ACE profiles at each height [ $100\% \times (ACE - SAGE II) / ACE$ ], plus the standard deviation in the mean at each height. Lines of the same color in the left and middle plots are coincident. Pairs of coincident profiles have been interpolated onto a common altitude scale and terminated at ACE’s lower altitude, which is higher than that of SAGE II profiles.

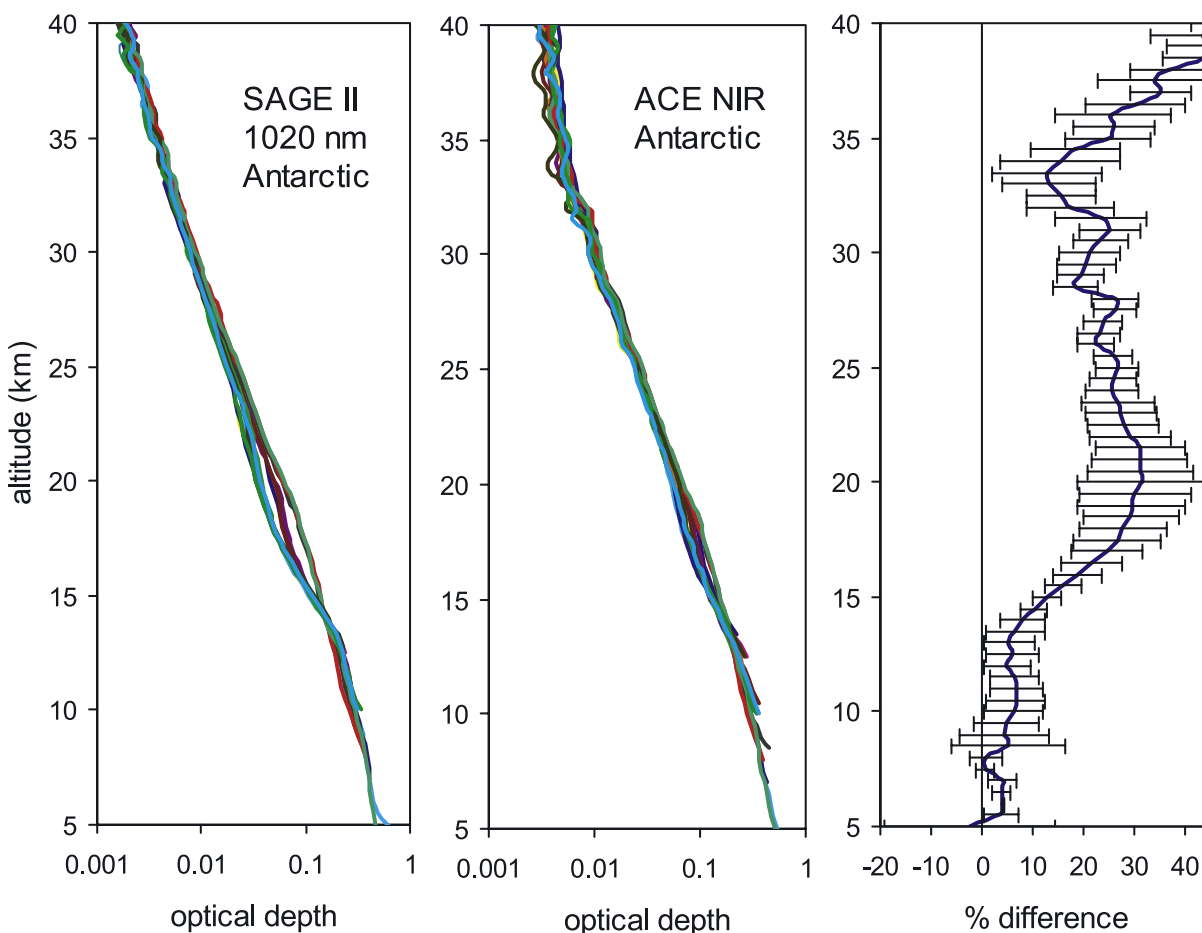


**Figure 14.** Similar to Figure 13 but comparing the 1020-nm channel from SAGE II and the ACE NIR imager.

height for a given pixel will increase during a sunrise and decrease during a sunset. The collection of transmission values and associated tangent heights derived from image pixels over an occultation gives the transmission profile along the line of sight, also called a slant path profile.

[21] The imagers view the entire solar disk throughout the occultation, so in principle all of the illuminated pixels can be used for the transmission profile. Currently, however, only three contiguous pixels centered on the coregistered field of view of ACE-FTS are used in the preliminary operational data processing. The three pixels are all at the same angular distance from the Earth's horizon, and so they all have the same tangent height. They are also located in the geometric center of the high sun image. The nominal field of view of the three pixels taken together is  $\sim 0.7$  mrad  $\times$   $0.234$  mrad (width by height), or a  $\sim 2$  km  $\times$   $0.7$  km footprint at the tangent point when viewing the limb. In comparison, the field of view of ACE-FTS is a 1.25-mrad diameter circle.

[22] Data processing begins with distinguishing the three image streams: i.e., deep space, high sun, and occultation or low sun. The high sun and occultation images are corrected for dark current and the anomalous linear intensity increase mentioned above. The high sun images are then averaged to produce a reference image with a very high signal-to-noise ratio (Figure 8). There are  $\sim 300$  high sun images on

average for an occultation, although only 144 are added together in the preliminary processing code in order to avoid the difficulty of deciding when the occultation starts. The reference high sun image is used as the divisor for the occultation images to produce transmission values.

[23] Because the intensity of the high sun is affected by limb darkening and the presence of sunspots, it is important to take intensity ratios between image pixels that look at the same portion of the sun. That is to say, a pixel looking at a certain area on the low sun, which appears deformed because of refraction, must be mapped to pixels in the high sun image that regard the same area. As an aid to mapping pixels between low sun and high sun images, the images are first rotated about their respective sun centroids so that the Earth's horizon is parallel to the imager horizontal axis (Figure 9). A premise of the mapping technique is that the width of the sun remains constant during an occultation; only the diameter in the direction of the local vertical to the Earth's surface appears compressed because of refraction. Thus the uncompressed widths across the sun's disk are more readily compared when they are aligned with imager rows after rotation (Figure 10). Uncertainties in measuring the radius of the sun in terms of pixel widths can be made worse when the pixels are at an arbitrary angle. It can also be difficult to determine where the edge of the rounded sun is when imaged by square pixels, particularly when signal

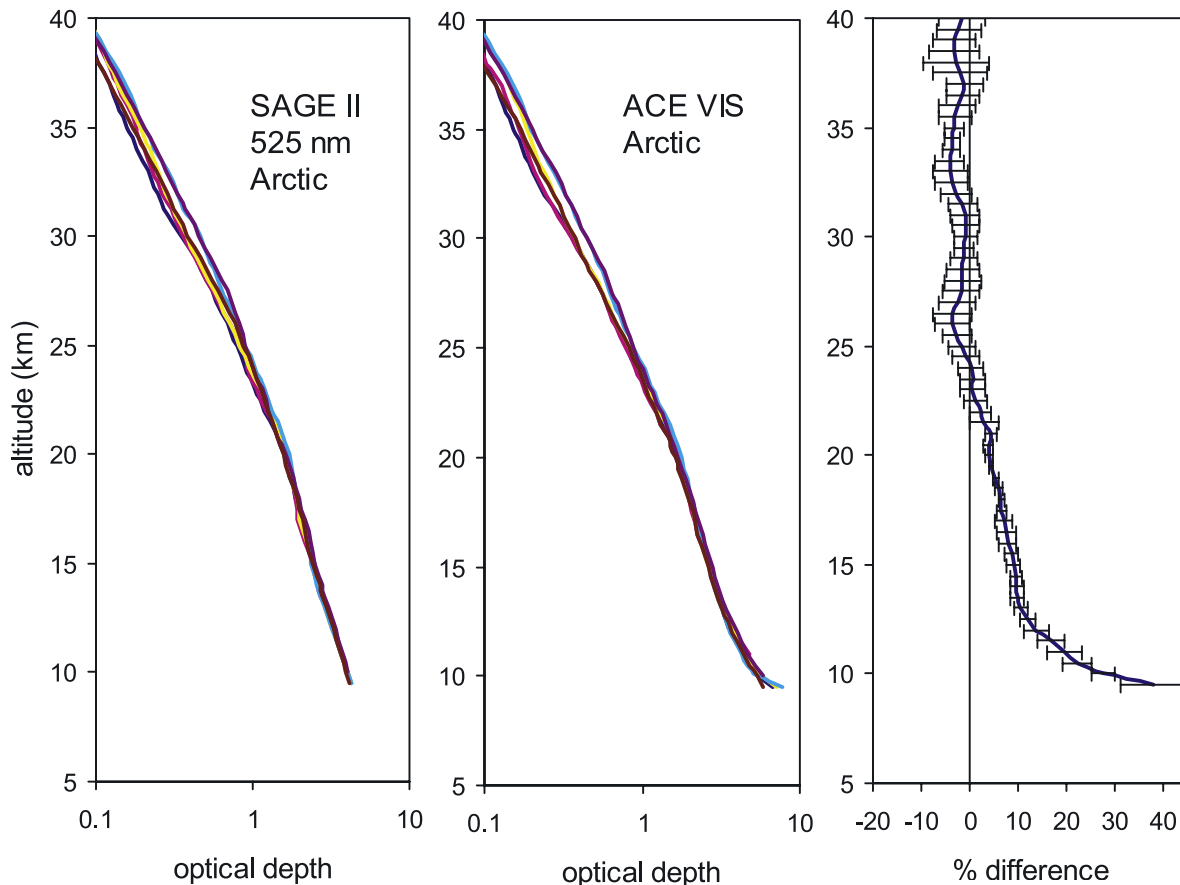


**Figure 15.** Plots of coincident optical depth slant path profiles from the 525-nm channel of SAGE II (left) and the ACE VIS imager (middle) from the Arctic on 22 March 2005. Six profiles are plotted in each case. The plot on the right hand side shows the average difference between the SAGE II and ACE profiles at each height [ $100\% \times (\text{ACE} - \text{SAGE II}) / \text{ACE}$ ], plus the standard deviation in the mean at each height. Lines of the same color in the left and middle plots are coincident. Pairs of coincident profiles have been interpolated onto a common altitude scale and terminated at ACE's lower altitude, which is higher than that of SAGE II profiles.

levels decline in low sun images. Rotating a square pixel into another square pixel at an angle of rotation other than a multiple of 90 degrees requires interpolation of pixel intensities, which is done by using the cubic convolution scheme of Keys [1981] with the free parameter of the piecewise spline set equal to  $-1$ . The angle of rotation is the angle made by MAESTRO's slit as coregistered on the imagers because the spacecraft attitude is controlled to maintain MAESTRO's slit parallel to the horizon.

[24] In general, the apparent vertical compression of the sun means that one pixel in the rotated low sun image is mapped to multiple pixels in the same column of the rotated high sun image. The average intensity among these multiple pixels is then used as the divisor to get a transmission value. The pixel-mapping procedure is not yet operational. In the preliminary version of the processing code, an approximation is used which sidesteps the pixel mapping; the pixel in the center of the coregistered ACE-FTS field of view from the reference high sun image is used as the divisor for all occultation images. The approximation is valid, within certain limits, because in the preliminary processing code only pixels coregistered with the center

of the ACE-FTS field of view are being analyzed. They happen to lie in the center of the high sun image, and in the high sun the intensity is relatively flat in the center over a circular area with a diameter of  $\sim 20\%$  of the sun's total diameter (Figure 8). Thus as long as an analyzed pixel in a low sun image is only mapped to 20% of the pixels in the corresponding column in the high sun image, the approximation holds. An apparent compression resulting in a vertical diameter that is 20% of the high sun diameter usually occurs when the apparent center of the sun has a tangent height of  $\sim 10$  km. Below this, the approximation somewhat underestimates transmission values. The next version of the processing code will implement a more general mapping scheme to replace the approximation and permit more pixels to be used in the analysis.

[25] The tangent heights that are assigned to the three analyzed pixels are interpolated from those that are assigned to ACE-FTS measurements by comparing the image timestamps with the ACE-FTS interferogram timestamps. The tangent heights for the ACE-FTS measurements are derived from a pressure/temperature analysis of  $\text{CO}_2$  volume mixing ratio in the FTS spectra [Boone *et al.*, 2005]. The relative

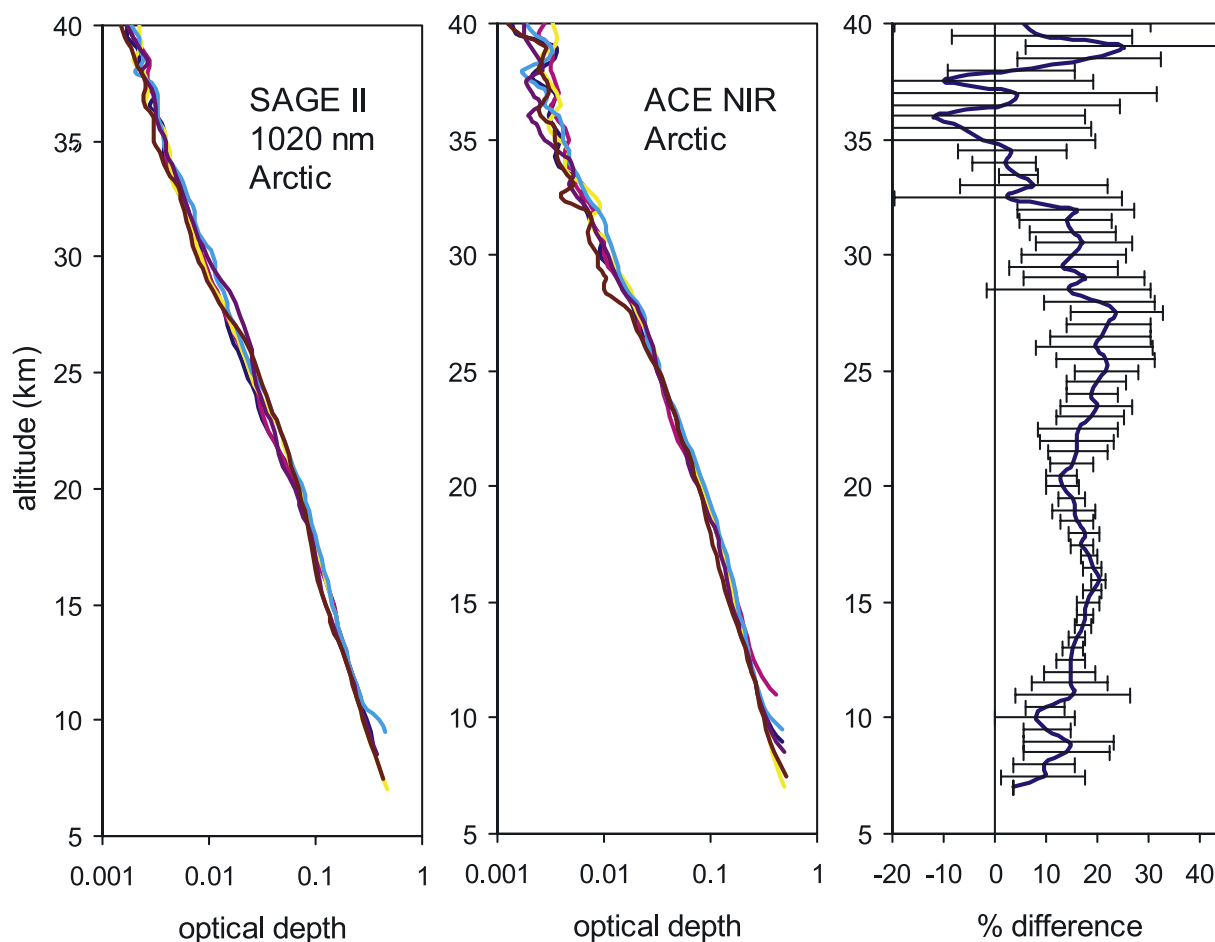


**Figure 16.** Similar to Figure 15 but comparing the 1020-nm channel from SAGE II and the ACE NIR imager.

accuracy of tangent height information from ACE-FTS, within a given occultation, is roughly 150 m. The absolute accuracy, i.e., altitude registration relative to local sea level, has yet to be determined. The inversion procedure used to produce altitude profiles is the same as for the FTS retrievals [Boone *et al.*, 2005]. The extinction profiles are gridded in altitude at 1-km intervals but are not extrapolated below the lower altitude limit of the transmission slant path profile. This is where the suntracker loses its lock on the sun because of the low signal, usually between 5–10 km tangent altitude. The profiles are capped at 74.5 km, well above a point where extinction becomes noticeable. Examples of retrieved altitude profiles of total atmospheric extinction are shown in Figure 11. Error bars are not shown because an error analysis is not included in the preliminary operational code.

## 5. Comparison With SAGE II Measurements

[26] Given the uncertainties concerning the imagers, one way to assess their performance is to compare their data with that of a similar satellite instrument. SAGE II is a seven-channel photometer that measured atmospheric aerosols and gas species by solar occultation. It flies at the same altitude as SCISAT-1 but in a lower inclination orbit of  $57^\circ$ . There were two periods for which both SAGE II and ACE

made observations in close proximity, defined here as being within 200 km and 1 hour. One set of measurements took place in the Antarctic on 19, 20, and 23 November 2004, and the other took place in the Arctic on 22 March 2005 (Figure 12). The 15 Antarctic coincidences happened over open ocean or just inland, with the ACE measurements taken between roughly  $-69^\circ$  and  $-70^\circ$  latitude, in all cases  $\sim 1^\circ$  south of the SAGE II measurements. In the Arctic, five coincidences occurred over mountainous terrain, and one occurred over the Canadian tundra. The ACE observations are at  $\sim 65^\circ$  latitude, between  $-0.1^\circ$  and  $1.5^\circ$  north of the SAGE II observations.

[27] The quantity being compared is the slant path profile of optical depth rather than inverted profiles in order to avoid differences based on inversion techniques. Thus differences between the two results will be due to instrumental and geophysical differences, as well as the data processing involved in deriving transmission values. The results are shown in Figures 13, 14, 15, and 16. Comparisons of the temperature profiles co-located with the slant path profiles are shown in Figures 17 and 18 to give some indication of the geophysical variability between the SAGE II and ACE measurement sites. All of the profiles are plotted between 5 and 40 km in altitude.

[28] Error bars are not plotted for the ACE optical depth profiles as the error analysis is still rudimentary. The error

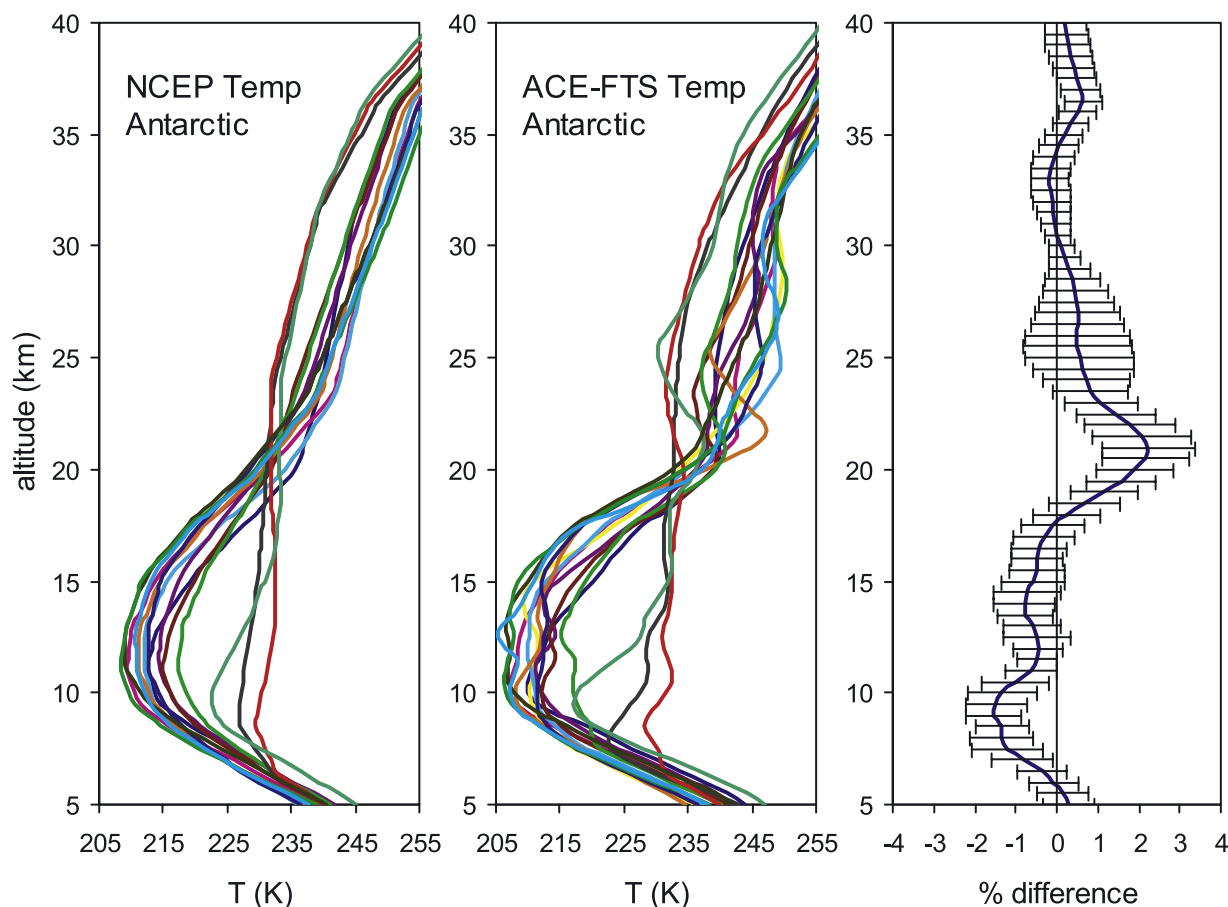


**Figure 17.** Temperature profiles corresponding to the times and locations of the Antarctic observations made by SAGE II (left), ACE (middle), and the difference between them,  $[100\% \times (\text{ACE} - \text{SAGE II}) / \text{ACE}]$ , (right). The SAGE II temperatures are interpolated from the National Centers for Environmental Prediction in the US, and the ACE temperatures are derived from a pressure/temperature analysis of ACE-FTS spectra. Lines of the same color in the left and middle plots are coincident.

bars for the SAGE II optical depths are generally too small to see on the scale plotted and therefore are not shown. The SAGE II temperatures are interpolated from temperature profiles provided by the National Centers for Environmental Prediction and have errors assigned of 3–5 K for the Antarctic temperatures below 35 km and 2–3 K for the Arctic temperatures below 35 km. Above 35 km, the error increases for all SAGE II temperatures. The ACE temperatures are derived from  $\text{CO}_2$  spectral features in the ACE-FTS spectra, as mentioned above. A couple of validation exercises concluded that the ACE-FTS temperatures agree with those of HALOE [McHugh *et al.*, 2005] and the Earth Observing System (EOS) Microwave Limb Sounder (MLS) [Froidevaux *et al.*, 2006] to within  $\sim 2$  K between 15–60 km in altitude.

[29] For the present purpose, we are looking for systematic differences between the SAGE II and ACE imager profiles that might indicate how the idiosyncrasies of the imagers affect our retrievals. The VIS/525 nm channel plots in Figures 13 and 15 indicate an absolute difference of less than 10% between SAGE II and ACE above 11 km for the Antarctic observations and above 13 km for the Arctic observations. Unfortunately, the difference switches sign

for the Arctic observations (Figure 15) at an altitude of 24 km, hampering a fast diagnosis.

[30] For the Antarctic observations (Figure 13), the ACE VIS data are a fairly constant 7% smaller than the SAGE II data between 25 and 40 km. Below 25 km, the difference is smaller and exhibits a bow-like structure between 15 and 25 km also seen in the NIR/1020 nm channel difference profile in Figure 14. These features likely reflect the same geophysical variation causing the large smooth difference in the temperature profiles centered on  $\sim 20$  km in Figure 17.

[31] For the NIR/1020 nm channel Antarctic observations in Figure 14, above the bow-like structure from  $\sim 25$  to 35 km, the average difference oscillates around  $\sim 20\%$ . Below the bow, the average difference oscillates around  $\sim 5\%$ . The pattern of larger difference above the bow than below is found as well in the temperature difference profile (Figure 17), and less markedly in the VIS/525 nm difference profile (Figure 13).

[32] The similarity in structure of the altitude profiles of the differences between VIS/525 nm, NIR/1020 nm and the temperatures (Figures 13, 14, and 17) is likely attributable to underlying geophysics and is motivation to look for a systematic difference between the SAGE II and ACE

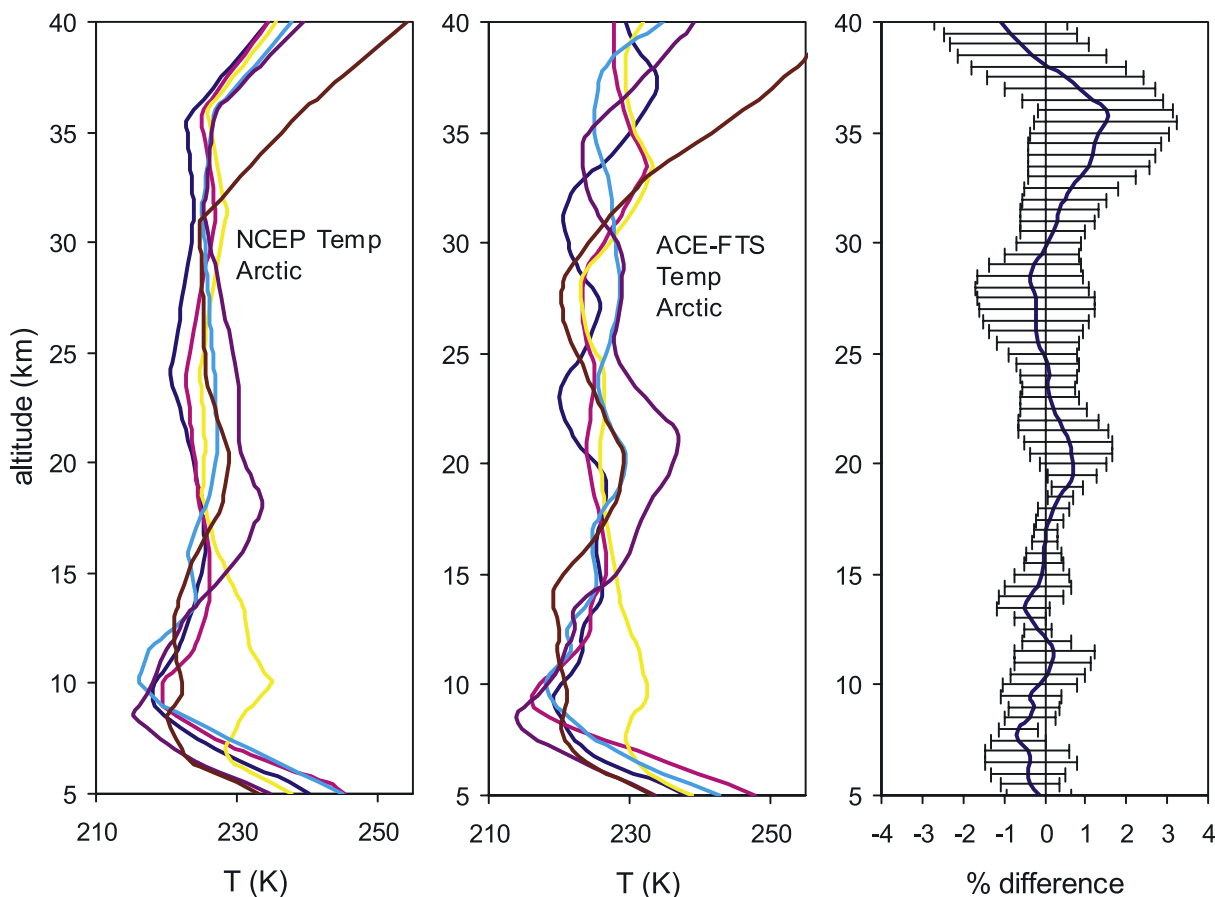


**Figure 18.** Similar to Figure 17 but for the Arctic observations.

imager data in the 30–34 km altitude region, where the temperature difference is closest to zero. If this simple correspondence holds, then the ACE VIS imager gives results that are  $\sim 5\%$  lower than SAGE II and the NIR imager gives results  $\sim 20\%$  higher because of effects other than geophysical variation.

[33] The geophysical component of the differences cannot be readily identified in the Arctic coincidences by looking at the plots alone. The difference profiles for VIS/525 nm, NIR/1020 nm, and the temperatures (Figures 15, 16, and 18) do not show the same broad correspondence in altitude with each other as do the Antarctic observations. This is perhaps because the Arctic observations are from more dynamically active conditions than the Antarctic, due to the topography, which leads to greater variability between observation sites. It is well known that small-scale spatial and temporal perturbations of the atmosphere are forced by orography, whereas mainly large-scale variations are found over the comparatively flat ocean. It can be noted, however, that the magnitude of the discrepancies between SAGE II and the ACE imager data from the Arctic are consistent with those from the Antarctic, with the possible exception of the VIS/525 nm difference below 13 km in the Arctic.

## 6. Conclusions

[34] In light of the instrument problems described above, the agreement between the SAGE II and ACE imager slant

path profiles is rather good, especially for the VIS imager data. It seems reasonable that the discrepancy between the NIR and the 1020 nm channel data is greater, given that the NIR images have more problems than the VIS. Even so, it is encouraging that the differences are on the order of 20%, as they could well have been much larger. The fact that ratios of pixel intensities are used to obtain transmission values rather than the intensities themselves ameliorates those problems which have the effect of altering a pixel's intensity by a constant, or almost constant, fraction. Cross-talk falls into this category, within limits, as might the lack of focus in the NIR imager.

[35] The biggest unknown is the effect of the shifting multiple images on the pixel intensities. This would likely manifest itself as an altitude-dependent effect, but it is not possible to identify it in the profiles presented here. It may be possible to estimate the size of the effect when more pixels are brought into the analysis. That is, when the analysis is performed for pixels viewing the same tangent height as the currently analyzed pixels but sampling a different part of the detector.

[36] There is more work to be done in refining the data analysis procedure and estimating uncertainties in the transmission values. Future plans also include comparisons of imager profiles with data from MAESTRO and SAGE III. Also, a comparison of the filter characteristics of the relevant SAGE II channels and the ACE imagers will determine whether the filter passbands contribute to the

differences in optical depth seen at these wavelengths. In the meantime, the initial comparisons are encouraging, but it should be remembered when using ACE imager data from the preliminary processing code that there is a discrepancy in the slant path optical depths of  $-5\%$  for the VIS and  $+20\%$  for the NIR when compared to SAGE II.

[37] **Acknowledgments.** We thank the Canadian Space Agency and the Natural Sciences and Engineering Research Council of Canada for funding this work. We also thank the NASA Langley Research Center (NASA-LaRC) and the NASA Langley Radiation and Aerosols Branch for the availability of SAGE II data and specifically thank Bill Chu, Nina Iyer, Sharon Burton, and Larry Thomason of NASA for their help.

## References

- Aikin, A. C., B. Woodgate, and H. J. P. Smith (1982), Atmospheric ozone determination by solar occultation using the UV spectrometer on the Solar Maximum Mission, *Appl. Opt.*, *21*(13), 2421–2424.
- Bernath, P. F., et al. (2005), Atmospheric Chemistry Experiment (ACE): Mission overview, *Geophys. Res. Lett.*, *32*, L15S01, doi:10.1029/2005GL022386.
- Boone, C. D., R. Nassar, K. A. Walker, Y. Rochon, S. D. McLeod, C. P. Rinsland, and P. F. Bernath (2005), Retrievals for the atmospheric chemistry experiment Fourier-transform spectrometer, *Appl. Opt.*, *44*(33), 7218–7231.
- Dodion, J., et al. (2007), Cloud detection in the upper troposphere—lower stratosphere region via ACE imagers: A qualitative study, *J. Geophys. Res.*, *112*, D03208, doi:10.1029/2006JD007160.
- Froidevaux, L., et al. (2006), Early validation analyses of atmospheric profiles from EOS MLS on the Aura Satellite, *IEEE Trans. Geosci. Remote Sens.*, *44*(5), 1106–1121.
- Fromm, M., J. Alfred, and M. Pitts (2003), A unified, long-term, high-latitude stratospheric aerosol and cloud database using SAM II, SAGE II and POAM II/III data: Algorithm description, database definition, and climatology, *J. Geophys. Res.*, *108*(D12), 4366, doi:10.1029/2002JD002772.
- Houghton, J. T., F. W. Taylor, and C. D. Rodgers (1984), *Remote Sounding of Atmospheres*, Cambridge Univ. Press, New York.
- Kester, W. (Ed.) (2005), *The Data Conversion Handbook*, Elsevier, New York.
- Keys, R. G. (1981), Cubic convolution interpolation for digital image processing, *IEEE Trans. Acoust., Speech, Signal Process.*, *29*, 1153–1160.
- Lucke, R. L., et al. (1999), The Polar Ozone and Aerosol Measurement (POAM III) instrument and early validation results, *J. Geophys. Res.*, *104*, 18,785–18,799.
- McElroy, C. T., et al. (2007), The ACE-MAESTRO instrument on SCISAT: Description, performance, and preliminary results, *Appl. Opt.*, in press.
- McHugh, M., B. Magill, K. A. Walker, C. D. Boone, P. F. Bernath, and J. M. Russell III (2005), Comparison of atmospheric retrievals from ACE and HALOE, *Geophys. Res. Lett.*, *32*, L15S10, doi:10.1029/2005GL022403.
- Razavi, B. (2001), *Design of Analog CMOS Integrated Circuits*, McGraw-Hill, New York.
- Rinsland, C. P., et al. (2006), First space-based observations of formic acid (HCOOH): Atmospheric chemistry experiment austral spring 2004 and 2005 Southern Hemisphere tropical-mid-latitude upper tropospheric measurements, *Geophys. Res. Lett.*, *33*(23), L23804, doi:10.1029/2006GL027128.
- Russell, J. M., III, L. L. Gordley, J. H. Park, S. R. Drayson, D. H. Hesketh, R. J. Cicerone, A. F. Tuck, J. E. Frederick, J. E. Harries, and P. J. Crutzen (1993), The Halogen Occultation Experiment, *J. Geophys. Res.*, *98*, 10,777–10,797.
- Russell, P. B., and M. P. McCormick (1989), SAGE II aerosol data validation and initial data use: An introduction and overview, *J. Geophys. Res.*, *94*, 8335–8338.
- Thomason, L. W., and G. Taha (2003), SAGE III aerosol extinction measurements: Initial results, *Geophys. Res. Lett.*, *30*(12), 1631 doi:10.1029/2003GL017317.

P. F. Bernath, Department of Chemistry, University of York, York, United Kingdom.

C. D. Boone, M. Butler, K. L. Gilbert, S. D. McLeod, and R. Skelton, Department of Chemistry, University of Waterloo, Waterloo, Ontario, Canada. (kathy.gilbert@sympatico.ca)

F. Chateaufneuf and M.-A. Soucy, ABB, Remote Sensing Industry, 585 Charest East, Suite 300, Québec City, Québec, Canada.

D. N. Turnbull, Department of Physics and Astronomy, The University of Western Ontario, London, Ontario, Canada.

K. A. Walker, Department of Physics, University of Toronto, Toronto, Ontario, Canada.